



Enhanced oxygen storage capacity of $\text{Ce}_{0.65}\text{Hf}_{0.25}\text{M}_{0.1}\text{O}_{2-\delta}$ (M = rare earth elements): Applications to methane steam reforming with high coking resistance



D. Harshini^a, Dae Hyung Lee^{a,b}, Jihoon Jeong^a, Yongmin Kim^a, Suk Woo Nam^{a,c},
Hyung Chul Ham^{a,b}, Jong Hee Han^a, Tae-Hoon Lim^a, Chang Won Yoon^{a,b,*}

^a Fuel Cell Research Center, Korea Institute of Science and Technology, Seoul 136-791, Republic of Korea

^b Clean Energy and Chemical Engineering, University of Science and Technology, Daejeon, Republic of Korea

^c Green School, Korea University, 145 Anam-ro, Seongbuk-gu, Seoul 136-701, Republic of Korea

ARTICLE INFO

Article history:

Received 13 June 2013

Received in revised form 16 October 2013

Accepted 13 November 2013

Available online 21 November 2013

Keywords:

Ceria–Hafnia

Oxygen storage capacity

Rare earth element

Steam reforming of methane

Coking resistance

ABSTRACT

To develop efficient materials possessing high oxygen storage capacity (OSC) for a number of catalytic applications, ceria–hafnia based metal oxides, $\text{Ce}_{0.65}\text{Hf}_{0.25}\text{M}_{0.1}\text{O}_{2-\delta}$, (CH-M, M = Tb, Sm, Nd, Pr, and La), were prepared by the EDTA-citrate method. The structural and textural properties of the as-synthesized materials were characterized by X-ray diffraction (XRD), Brunauer–Emmett–Teller (BET) analyses, Raman spectroscopy, X-ray photoelectron spectroscopy (XPS), and high resolution transmission electron microscopy (HRTEM). These analyses indicated that the doping of the rare earth elements could potentially induce enhanced OSC compared to the undoped CeO_2 – HfO_2 solid solution, and particularly, the CH-Pr, CH-La, and CH-Tb materials were suggested to possess greater OSC than other CeO_2 – HfO_2 based solid solutions. The redoxability and size of the dopants were proposed to play a pivotal role in enhancing the OSC of the as-prepared materials. Soot oxidation experiments were further performed to examine the relative OSC of the ceria–hafnia based solid solutions and revealed that soot oxidation activities increased in the order of CH-Pr > CH-La > CH-Tb > CH-Nd > CH-Sm > CH (undoped material). To elucidate the effect of these materials on suppressing carbon coking, Ni/CH and Ni/CH-Pr catalysts were synthesized by a solvothermal method and their catalytic activities towards steam reforming of methane with steam to carbon ratios of 1–2 at 700 °C were carried out. The Ni/CH-Pr catalyst exhibited superior activity and stability over Ni/CH for the steam reforming of methane, which likely resulted from the enhanced oxygen mobility of the CH-Pr support.

Crown Copyright © 2013 Published by Elsevier B.V. All rights reserved.

1. Introduction

Owing to their high oxygen storage and transport capability, ceria (CeO_2) based materials have attracted significant attention for a wide range of catalytic applications including three-way catalysts [1], solid oxide fuel cells [2], hydrocarbon reforming catalysts [3], and water gas shift catalysts [4], and so forth. The oxygen storage capacity (OSC) is associated with the formation of oxygen vacancies along with their diffusion ability in ceria [5–7], which can further be enhanced by the incorporation of dopants into the ceria lattice [8–11]. In addition, such displacement of Ce with a dopant may also help prevent sintering of ceria at high temperatures. In this context, a transition metal and/or rare earth metal based dopant has extensively been employed to increase the thermal stability

and the OSC of ceria [12,13]. In particular, zirconia has proved to be an excellent dopant to improve the oxygen mobility of bulk ceria as well as to prevent the sintering of ceria at high temperatures [14,15]. Due to its smaller ionic radius than Ce^{4+} , the doping of this nonreducible, isovalent zirconium cation (Zr^{4+}) into ceria can induce the distortion and expansion of the CeO_2 lattice to facilitate the generation of oxygen vacancies [14].

A similar strategy to enhance the OSC of ceria has been adopted using hafnium element as an additive into ceria, producing ceria–hafnia solid solution [16]. Moreover, redox properties of ceria–hafnia, ceria–terbia, and ceria–praseodymia materials were investigated [17]. Like zirconium ion (Zr^{4+} , ionic radius of 0.84 Å), the nonreducible, isovalent hafnium ion (Hf^{4+} , ionic radius of 0.83 Å) possesses smaller ionic radius than Ce^{4+} (ionic radius 0.97 Å), and therefore, utilization of the Hf element likewise induced the enhancement of the OSC from a $\text{Ce}_x\text{Hf}_y\text{O}_z$ material; i.e., the substitution of Ce with Hf sterically affects the ceria lattice to result facile reduction of Ce^{4+} into Ce^{3+} [16,18]. Despite the fact

* Corresponding author.

E-mail addresses: cwyoon@kist.re.kr, cw.yoon@ust.ac.kr (C.W. Yoon).

that the OSC of the $\text{CeO}_2\text{--HfO}_2$ based materials can be higher than those of CZ solid-solutions [19], however, there are only few reports concerning the development of ceria–hafnia (**CH**) solid-solutions for the catalytic applications to date. Given the fact that doping of a trivalent rare earth element (RE^{3+}) ion can replace a Ce^{4+} ion to generate one oxygen vacancy by balancing charge, utilization of RE may further enhance the OSC property of the $\text{CeO}_2\text{--HfO}_2$ based materials. In particular, doping with a RE element that can exist in +3 oxidation state could potentially yield a $\text{CeO}_2\text{--HfO}_2$ based material possessing remarkably high OSC.

In this research, a series of M doped-CH solid-solutions (M = rare earth elements; Tb, Sm, Nd, Pr and La) were initially prepared to develop highly stable supports for catalysis, followed by characterization with differential temperature analysis-thermogravimetric analysis (DTA-TGA), X-ray diffraction (XRD), Raman spectroscopy, and X-ray photoelectron spectroscopy (XPS). These techniques provided valuable insight for the steric influence of the doped RE elements as well as for the electronic effect of some additives by monitoring changes in oxidation states of the doped element within a M doped-CH oxide as well as at the surface of the material. The relative OSC of the as-synthesized materials were examined experimentally by soot oxidation and compared to the spectroscopic results. Finally, Ni-based catalysts supported onto $\text{CeO}_2\text{--HfO}_2$ and Pr-doped $\text{CeO}_2\text{--HfO}_2$ materials were prepared and their catalytic stabilities were tested by methane steam reforming reactions.

2. Experimental

2.1. The preparation of materials

All catalyst powders were prepared using the EDTA-citrate method [20]. Metal nitrates were employed as desired metal precursors for supports except for HfCl_4 . A 10 g-scale preparation for $\text{CeO}_2\text{--HfO}_2$ (**CH**) is described below as an example. Cerium nitrate ($\text{Ce}(\text{NO}_3)_3 \cdot 6\text{H}_2\text{O}$, 20.2 g, 46.6 mmol) was dissolved in deionized water (466 mL), followed by mixing into an aqueous solution of hafnium chloride (HfCl_4 , 4.98 g, 15.5 mmol) at room temperature. EDTA (18.0 g, 61.6 mmol) dissolved in an aqueous NH_3 solution was then dropped into the mixed solution, followed by the addition of solid citric acid (17.8 g, 92.4 mmol) upon stirring. Molar ratio of total metal ions (Ce + Hf), EDTA, and citrate is 1.0:1.0:1.5, respectively. NH_4OH was used to adjust the pH of the solution to a desired value of 6. The solution was then heated above 80°C slowly and became transparent yellow gel. The gel was placed in an oven preheated at 200°C for 12 h to convert into solid powders. Next, the powders were calcined at 600°C for 3 h in air to yield CH solid solution. The preparation method for M-doped **CH** samples is as follows: The M doped **CH** samples (**CH-M**, M = Tb, Sm, Nd, Pr, and La) were prepared by the following procedure. As an example, **CH-Tb** was synthesized by mixing aqueous solutions of cerium nitrate ($\text{Ce}(\text{NO}_3)_3 \cdot 6\text{H}_2\text{O}$, 18.4 g, 42.3 mmol), hafnium chloride (HfCl_4 , 5.21 g, 16.3 mmol), and terbium nitrate ($\text{Tb}(\text{NO}_3)_3 \cdot 5\text{H}_2\text{O}$, 2.85 g, 6.54 mmol) at room temperature. EDTA (19.0 g, 64.8 mmol) dissolved in an aqueous NH_3 solution was then dropped into the mixed solution, followed by the addition of solid citric acid (18.7 g, 97.3 mmol) upon stirring. Molar ratio of total metal ions (Ce + Hf + Tb) to EDTA and to citrate is approximately 1.0:1.0:1.5. NH_4OH was employed to adjust the pH of the solution to a desired value of 6. The solution was then heated above 80°C to produce transparent brownish gel. The gel was placed in an oven preheated at 200°C for 12 h to give solid powders. Finally, the powders were calcined at 600°C for 3 h in air to yield CH-Tb solid solution. The synthesized powders were designated as **CH** (ceria–hafnia), **CH-Tb** (Tb doped CH), **CH-Sm** (Sm doped CH), **CH-Nd** (Nd doped CH), **CH-Pr** (Pr doped CH), and **CH-La** (La doped CH), respectively.

To examine the durability of Ni-based catalysts supported onto **CH-M**, **CH-Pr** was chosen since this material exhibited superior oxygen storage capacity (OSC), compared to other **CH-M** (*vide infra*). The deposition of nickel on the **CH** and **CH-Pr** supports was achieved by a solvo-thermal synthesis to produce 10 wt% Ni supported onto **CH** (**Ni/CH**) and Ni supported onto **CH-Pr** (**Ni/CH-Pr**), respectively [20]. The solvo-thermal procedure for the preparation of Ni/CH as an example was described as follows: $\text{Ni}(\text{NO}_3)_2 \cdot 6\text{H}_2\text{O}$ (2.50 g, 8.60 mmol) was dissolved in tetrahydrofuran (THF, 100 mL), followed by adding into the CH powder (4.5 g). The heterogeneous mixture was then agitated at room temperature for 1 h and further dried at 100°C . The resulting products were calcined at 450°C for 5 h in air.

2.2. Characterization of catalysts

During the preparation method, the evaporation of water from a mixture of $\text{Ce}(\text{NO}_3)_3 \cdot 6\text{H}_2\text{O}$ and HfCl_4 with EDTA at 80°C produced a deep yellow gel. This prepared gel was initially characterized by DTA-TGA using a TG-DSC analyzer, Q-600 at a heating rate of $10^\circ\text{C}/\text{min}$ in air. The Brunauer–Emmett–Teller (BET) surface areas of the as-prepared materials were analyzed by a micrometrics Quantachrome instrument.

Powder XRD patterns were obtained with a Rigaku X-ray diffractometer, using $\text{Cu K}\alpha$ radiation with wavelength of 1.542 \AA at 40 kV and 20 mA. The XRD diffraction patterns were taken in the 2θ range of $20\text{--}80^\circ$ at a scan speed of $0.04^\circ/\text{s}$. Phase identification was carried out by comparison with JCPDF database cards. The mean crystallite size (D_{XRD}) were calculated by the Scherrer's equation, $D = (0.9\lambda)/(\beta \cos\theta)$, where D is the crystallite size, λ is the wavelength of the radiation, β is the corrected peak width at the half-maximum intensity (FWHM), and θ is the peak position. The lattice parameter was calculated by a standard cubic indexation method with the intensity of the most prominent peaks using the relation of $a = d(h^2 + k^2 + l^2)^{1/2}$ where a is the lattice parameter and d is the interplanar spacing calculated from the Bragg equation.

Raman studies were further conducted using a Horiba Jobin Yvon Labram–Aramis Raman spectrometer equipped with an integral BX 41 confocal microscope. The radiation from a diode laser ($\lambda = 785 \text{ nm}$) with nominal output power of $\sim 0.5 \text{ mW}$ was used as an excitation source. Raman scattering was detected with 180° geometry using a multi-channel-air-cooled (-70°C) charge-coupled device (CCD) camera (1024×256 pixels). The Raman spectra were obtained in the frequency range corresponding to $1550\text{--}200 \text{ cm}^{-1}$. To obtain comparable data, the powder samples were dry pressed to form disks in a home-made mold and were then analyzed.

XPS analyses were performed under ultrahigh vacuum using PHI 5800 Versa probe instrument (Physical Electronics, USA). Charging of the samples was minimized by referencing the spectra to the C 1s line at BE 284.6 eV. The HRTEM studies were analyzed by Philips-CM30 transmission electron microscope (TEM) operated at 200 kV; samples for TEM analyses were dispersed in ethyl alcohol, followed by transferring into a holey 400 mesh copper grid. Specimen was examined under vacuum at room temperature. EDS/SEM (EDAX/SEM, XL-30 FEG ESEM, USA) is used for the compositional analyses.

2.3. The evaluation of catalytic activity for soot oxidation and SRM

To determine relative OSC of the as-synthesized supports, soot oxidation experiments were carried out by thermo gravimetric analyses (TGA) using a TG-DSC, Q-600 instrument. Soot used in this study was carbon black purchased from Degussa. In a typical experiment, a mixture of soot and **CH-M** support with a weight ratio of

1:4 was ground in an agate mortar to ensure a ‘tight contact’ condition following an oxidation reaction [22]. The resulting mixture (13–15 mg) was placed in a TGA crucible and heated up to 1000 °C with a heating rate of 10 °C/min under 100 mL/min of air flow [22].

To validate a hypothesis that a catalyst possessing improved OSC has high catalytic stability toward a reaction involving carbon coking, activities for the steam reforming of methane (SRM) over **Ni/CH** and **Ni/CH-Pr** catalysts were further examined in a fixed-bed reactor (inner diameter, 9 mm; material, quartz) at atmospheric pressure. The inlet pressure of the reactor was measured using a commercial pressure sensor/gauge (PSA-1, Autonics). The reactor with a prepared catalyst (weight, 0.2 g; volume, 0.3 mL) was heated in an electric furnace equipped with a temperature controller (Hanyong Nux. co. Ltd). The heating and cooling rates were maintained at 5 °C/min. Prior to a desired reaction, an as-synthesized catalyst was reduced *in situ* by flowing H₂ at 700 °C for 5 h with a flow rate of 50 mL/min. The reactor was flushed with N₂ for 30 min and then exposed to the reacting gas, a mixture of methane, steam, and N₂ with total flow rate of 85 sccm and N₂ flow rate of 34 sccm at 700 °C, while changing steam to carbon (S/C) ratio from 2 to 1. To be specific, at S/C ratio of 2, 1.5 and 1, molar concentrations of reactants (CH₄:H₂O:N₂) were 20:40:40, 24:36:40, and 30:30:40 (mol%), respectively while sustaining gas hourly space velocity (GHSV) at 10,000 h⁻¹. Flow rates of all reacting gases were controlled by a mass flow controller (MKP series, TSC-110 model). A cold trap at the outlet of the reactor was employed to condense water produced during the reactions. Mixtures of the effluent gas were analyzed by an online gas chromatograph (Agilent 7890A) equipped with two capillary columns (PorapakQ and molecular sieve) as well as two thermal conductivity detectors (TCDs). N₂ was used as a tie component.

2.4. Determination of OSCs using thermogravimetric analyses

The oxygen storage capacities (OSC) of the supports were determined by thermal analyses using various temperatures ranging from 300 °C to 750 °C, according to a literature procedure [21]. Changes in the weight of the sample were measured by thermogravimetry (TG analyzer, Q50) under cyclic heat treatment in flowing dry air. First of all, a desired sample was heated to 750 °C, followed by cooling to 150 °C. The sample was then re-heated to 750 °C with consecutive cooling to 150 °C. The heating and cooling rates were 5 °C/min. The oxygen storage capacity (δ) was calculated using the weight loss of the sample following the second heating cycle.

2.5. Measurement of weight change

Weight changes in Ni based catalysts upon increasing temperature under the flow of CH₄ were monitored by a home-made apparatus [23], surrounded by an open-ended, high-temperature electrical furnace that can heat the samples to 1000 °C. The **Ni/CH** and **Ni/CH-Pr** powders (0.1 g, each) were placed on an alumina crucible and covered with a quartz tube. The flow rates of methane and hydrogen gases were controlled by mass flow controllers (MFCs, TSC-210, MKP). Changes in weight of the **Ni/CH** and **Ni/CH-Pr** catalysts were monitored as a function of time. Other materials (alumina and quartz) except for the catalysts showed no activity toward carbon coking. Prior to the experiments, both the catalysts were reduced using H₂ (30 mL/min) at 700 °C for 2 h. Methane (200 mL/min) was purged into the reactor at 700 °C for 20 h. The reacting gases were flowed vertically from the top to the bottom. Total weight of each sample, including the powder, and the alumina crucible was measured by an electronic weight sensor (UniBloc, Shimadzu).

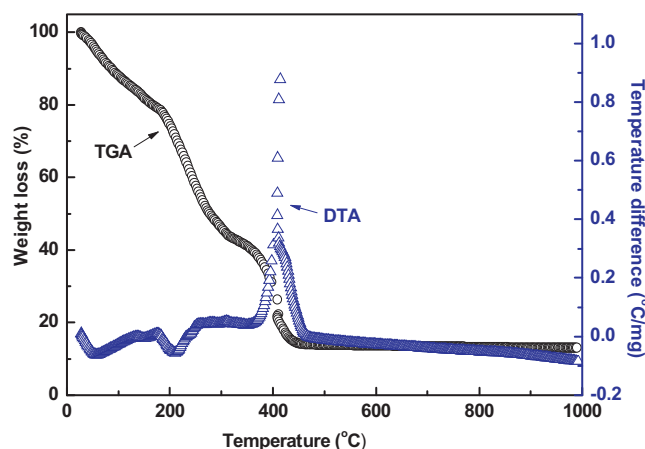


Fig. 1. The TG-DTA curve of the CH precursor pre-dried to a soft gel at 80 °C.

3. Results and discussion

3.1. DTA-TGA analyses of the as-synthesized **CH** material

Fig. 1 shows the DTA-TGA curves of the CeO₂-HfO₂ (**CH**) gel obtained from the mixture of Ce(NO₃)₃·6H₂O and HfCl₄ with the treatment of EDTA, citric acid, and ammonium hydroxide at 80 °C. The DTA curve (blue line) shows two major endothermic peaks; the peak centered at 50 °C is associated with the removal of superficial and structural water in the gel precursor [24] while the peak centered at 210 °C is related to the formation of EDTA complex [25]. The DTA profile also exhibits a strong and sharp exothermic peak centered at 415 °C, which likely resulted from the oxidation of the chelated complex along with the formation of metal oxides [26]. The TGA result (black line) shows the first weight loss of about 21% occurred during the heating step from room temperature to 200 °C, presumably due to the dehydration and decomposition of nitrates. From 200 °C to ca. 500 °C, a weight loss of about 65% was observed, which corresponds to the decarbonization of the residual organic compounds [26]. No endothermic or exothermic peaks were found from 500 °C to 1000 °C in the DTA curve, with little weight loss being observed. These results clearly indicate that all the samples calcined at 600 °C have no impurities after the required phase formation through calcinations.

3.2. XRD analyses of the as-prepared supports

The XRD patterns of the synthesized CeO₂-HfO₂ (**CH**), and M-doped CeO₂-HfO₂ (**CH-M**) materials calcined at 600 °C are shown in Fig. 2. The XRD patterns of all samples are symmetric in nature with the typical cubic fluorite structure [27]. Furthermore, no peaks corresponding to the individual oxides of HfO₂, Tb₄O₇, Sm₂O₃, Nd₂O₃, Pr₆O₁₁, and/or La₂O₃ were observed, indicating the formation of solid solutions in the as-prepared materials. Compared to that of the **CH** sample, the 2 θ values associated with CeO₂ (111) at ca. 29° (corresponding lattice parameter = 5.4 Å, [27]) of M-doped **CH** shifted into lower angles (Table 1). This result again supports the formation of solid solutions and is associated with the expansion of the crystal lattice induced by the doping of an element with the larger ionic radius than the Ce⁴⁺ ions. The lattice parameters of all the M-doped **CH** samples increased with increases in the ionic radius of the dopant: **CH-La** > **CH-Pr** > **CH-Nd** > **CH-Sm** > **CH-Tb** > **CH**. Note that the ionic radii of these additives increase in the following order: La³⁺ (1.16 Å) > Pr³⁺ (1.13 Å) > Nd³⁺ (1.11 Å) > Sm³⁺ (1.08 Å) > Tb³⁺ (1.04 Å) [28–30]. The incorporation of the rare earth metals thus likely induced the distortion of the CeO₂-HfO₂ lattice, enhancing the OSC of the doped materials. The crystallite sizes of

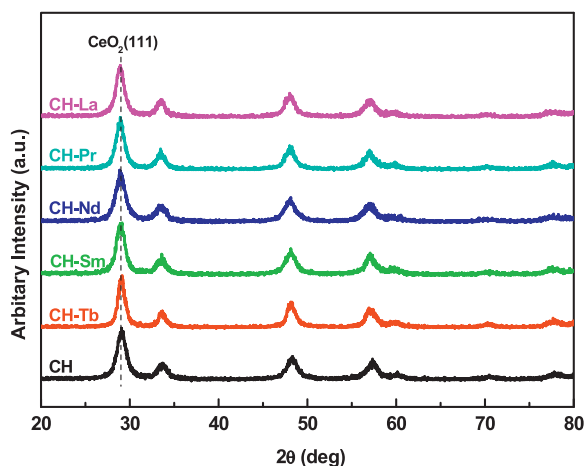


Fig. 2. XRD patterns of the as-synthesized materials (**CH-M**, M = Tb, Sm, Nd, Pr, and La).

Table 1
Surface areas, crystallite sizes, and lattice parameters of the as-prepared materials.

Support	BET surface area (m ² /g)	Crystallite size (nm)	Lattice parameter (Å)	2θ
CH	43.5	12.21	5.315	29.07
CH-Tb	56.9	16.25	5.318	29.06
CH-Sm	58.1	13.04	5.336	28.96
CH-Nd	63.8	11.70	5.337	28.95
CH-Pr	70.8	13.39	5.344	28.91
CH-La	78.3	13.70	5.347	28.90

all samples were calculated to be 11–16 nm. The compositions of the as-synthesized materials were confirmed by SEM-EDS analyses (Table 2). The TEM images of all the M-doped **CH** samples were presented in Fig. S1 (Supporting Information).

3.3. Qualitative measurement of OSC using Raman spectroscopy

Raman Spectroscopy is a useful technique to gain insight into the relative extent of OSC in oxide materials because it is sensitive to M–O bond arrangement and/or lattice defects [31]. Since the mobility of oxygen atoms in a crystal lattice is critical for ionic/electronic conductors as well as for redox catalysts, it is necessary to understand the structural details of a crystal lattice. In this context, we determined the relative OSC of the as-synthesized materials using Raman spectroscopy. As depicted in Fig. 3, a strong band centered at ca. 465 cm^{−1} was observed for a CH-based sample. For pure ceria, a

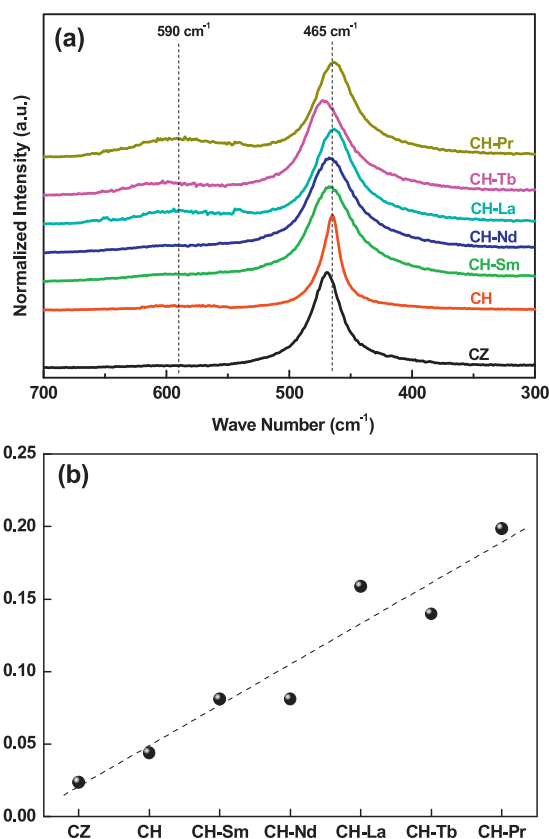


Fig. 3. (a) Raman spectra and (b) I_{590}/I_{465} ratios of the as-synthesized materials.

peak centered at 465 cm^{−1} is known to be attributed to symmetric breathing mode of oxygen ions bounded by Ce ions (degenerate F_{2g} mode) [11]. Upon doping, the peak was shifted into either higher or lower frequencies (Fig. 3a). Even though these shifts of the peak positions are associated with a number of factors [32], the shifts in this F_{2g} mode from 465 cm^{−1} clearly suggest the formation of solid solutions [18], which is also evidenced by our XRD studies.

In addition to this strong band, a band centered at ca. 590 cm^{−1}, attributable to a non-degenerate longitudinal optical mode (LO mode) [33], is also found (Fig. 3a). Recently, Luo et al. [34] reported that this band is closely associated with the oxygen vacancies in the ceria lattice, and a higher ratio of I_{590}/I_{465} , where I_{590} and I_{465} are peak intensities of the band centered at 590 cm^{−1} and at 465 cm^{−1}, respectively, likely indicates a higher relative quantity of oxygen vacancies. In the series of M-doped materials, the I_{590}/I_{465} ratios for **CH-Pr**, **CH-Tb**, and **CH-La** are found to be high, indicating that these materials possess high OSC with respect to other oxides (Fig. 3b). Since La only possesses +3 oxidation state, the improved OSC of **CH-La** may likely originate from the high ionic radius of La³⁺ which induces distortions in the **CH** lattice [35]. In contrast, the enhanced OSCs for **CH-Tb** and **CH-Pr** may come from the existence of Tb^{3+/4+} and Pr^{3+/4+} species to increase oxygen vacancies in the CeO₂–HfO₂ lattice [11]. In the case of **CH-Pr**, the high ionic radius of Pr³⁺ additionally played an important role in enhancing the OSC of the **CH-Pr**. Other M-doped **CH** materials, **CH**, **CH-Sm**, and **CH-Nd** showed relatively low I_{590}/I_{465} ratios, suggesting that these supports possess lower OSC compared to **CH-Pr**, **CH-Tb**, and **CH-La**. Notably, a recent UV–Raman spectroscopic study suggests that utilization of a laser with a wavelength of $\lambda = 785$ nm determined bulk OSC properties of the rare-earth elements doped ceria materials, rather than those at the surface [36]. Since deposited carbon species would initially react with surface oxygen ions to enhance the stability of a catalyst during a reforming reaction, different types of surface

Table 2
Compositions of the as-synthesized supports determined by SEM-EDS analyses.

Material	Element	Mole %
Ce _{0.75} Hf _{0.25} O ₂	Ce	74.4
	Hf	25.6
Ce _{0.65} Hf _{0.25} Tb _{0.1} O ₂	Ce	65.7
	Hf	24.4
	Tb	9.8
	Ce	65.0
Ce _{0.65} Hf _{0.25} Sm _{0.1} O ₂	Hf	24.8
	Sm	10.1
	Ce	63.9
	Hf	25.8
Ce _{0.65} Hf _{0.25} Nd _{0.1} O ₂	Nd	10.2
	Ce	64.2
	Hf	24.7
	Pr	11.1
Ce _{0.65} Hf _{0.25} La _{0.1} O ₂	Ce	64.4
	Hf	24.9
	La	10.6

characterization methods (e.g., X-ray photoelectron spectroscopy) may need to determine the relative extent of surface OSC in these materials.

3.4. XPS analyses of the as-prepared materials

Redoxability of a rare-earth element as a dopant (M^{3+}/M^{4+}) is one of the important properties for enhancing OSC of an oxide material because the surface concentration of M^{3+} species is closely linked with OSC. The oxidation state of a dopant located at the surface can readily be determined by XPS, and in this context, the XPS analyses were performed on the M-doped **CH** samples calcined at 600 °C. The results corresponding to Ce 3d, O 1s, and Hf 4f of all samples are shown in Fig. 4 and XPS spectra of Tb 4d of **CH-Tb** and Pr 3d of **CH-Pr** are depicted in Fig. 5, respectively. Firstly, owing to two multiplicities of 3/2 (u) and 5/2 (v), the Ce 3d spectra showed five spin orbit doublets [36,37]. These two sets of spin-orbit multiplets are labeled as $v_o, v, v', v'', u_o, u, u', u''$ and u''' , respectively, according to the literature [12]. Note that the labels of v, v', u, u'' are attributed to Ce^{4+} while those of u_o, v' and u' come from Ce^{3+} [37]. The Ce 3d profile of all the prepared materials depicted in Fig. 4a showed peaks corresponding to v, v'', u, u', u'' , and u_o , indicating the presence of Ce in both 4+ and 3+ oxidation states at the surface of all the supports employed in this study. The O 1s core level XPS profiles (Fig. 4b) of all the samples are noted by a broad peak centered at 528.7 eV, which is attributed to the lattice oxygen associated with **CH-M** ($M = Tb, Sm, Nd, Pr, \text{ and } La$) and this observation is consistent with the peak related to the lattice oxygen of the Pr-doped cerium oxide [11]. These peaks for the **CH-Pr** and **CH-La** materials are moderately shifted into higher binding energies than **CH**, indicating the presence of greater quantities of Ce^{3+} at the surface in these samples [30]. The peak centered at 531 eV, observed for all the synthesized materials, could be associated to absorbed water and/or carbonates [11]. The Hf 4f XPS spectra are also presented in Fig. 4c. Two peaks at 16.1 eV and at 17.5 eV observed for the **CH** and M-doped **CH** materials are attributed to the Hf 4f_{7/2} and Hf 4f_{5/2} levels, respectively [38]. The differences in binding energy between these two components are calculated to be approximately 1.4 eV, indicating that Hf in the as-prepared materials existed in 4+ oxidation state [12].

The XPS patterns of Tb 4d and Pr 3d of **CH-Tb** and **CH-Pr**, respectively, are further illustrated in Fig. 5. The Tb 4d core level spectrum of the **CH-Tb** sample showed peaks in a range from 140 eV to 170 eV. A pronounced peak centered at 150 eV extending to 160 eV indicates the existence of multi-oxidation states of Tb (Tb^{3+} and Tb^{4+}) in the **CH-Tb** sample (Fig. 5a) [12,30]. The Pr 3d spectrum of the **CH-Pr** sample seems to afford four peaks at binding energies centered on 928.1, 932.4, 947.3, and 952.7 eV, respectively. The signals at 952.7 and 932.4 eV are related to Pr^{4+} and the peaks at 947.3 and 928.1 eV are associated with Pr^{3+} , based on the previous results [11,39]. These results clearly indicate the existence of Pr species in the **CH-Pr** material with two possible oxidation states (Pr^{3+} and Pr^{4+}). Unlike the Tb and Pr dopants, the Sm, Nd, and La elements existed in only 3+ oxidation states, as evidenced by the XPS analyses.

The surface enrichment of cerium can be estimated from the Ce/Hf ratio calculated using the Ce 3d and Hf 4f atomic data obtained from the XPS analyses [40]. The calculated atomic concentrations and atomic ratios at the surface of the materials are listed in Table 3. The surface Ce/Hf ratios in the as-synthesized supports were found to be close to the theoretical value of 2.6 (in parentheses), indicating that the as-prepared supports formed in a homogeneous manner with regular Ce and Hf distributions. Notably, the **CH-Pr** support exhibited the highest surface Ce/Hf ratio among the M-doped **CH** materials. In addition, this **CH-Pr** support is also calculated to possess the highest Pr/(Ce + Hf) ratio on

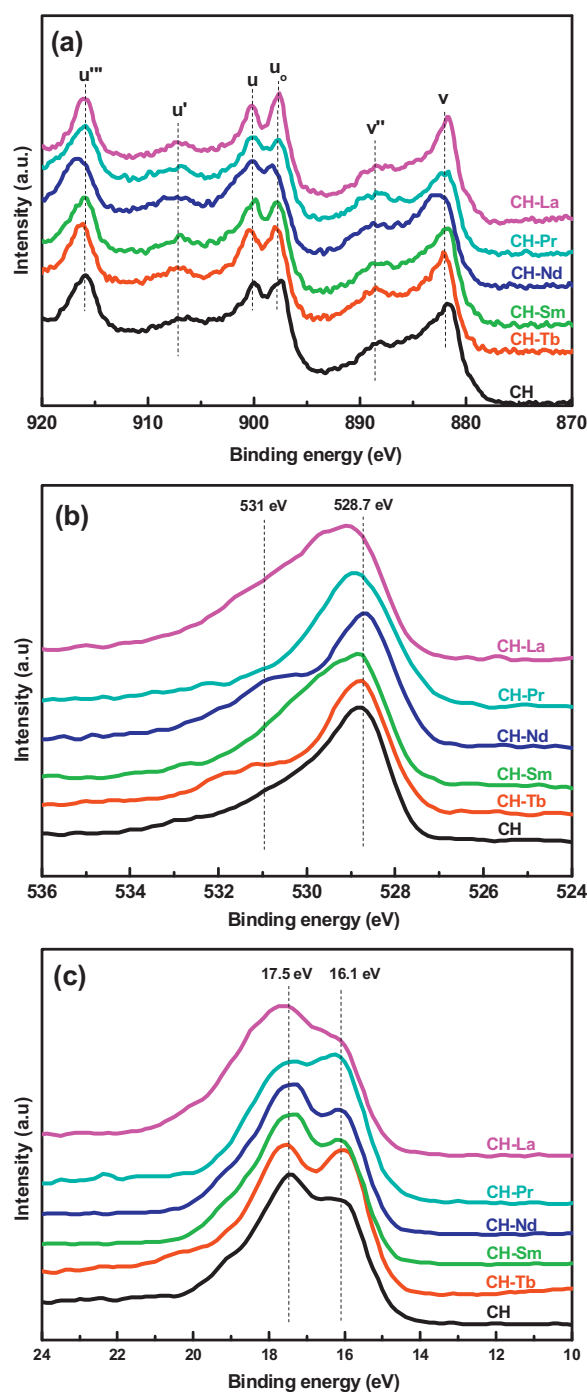


Fig. 4. XPS patterns of the M-doped CH materials following calcination at 600 °C: (a) Ce 3d, (b) O 1s, and (c) Hf 4f.

its surface. These results suggest that this material could have the highest OSC among the supports employed in this study, which is consistent with the XPS analyses (vide supra).

3.5. Measurement of the relative OSC of the as-developed materials: Soot oxidation

The presence of active oxygen species in a support plays a key role in preventing catalyst deactivation via carbon deposition. The relative ability to generate active oxygen species in a support is closely associated with OSC of the material. If hydrocarbon

Table 3
Surface atomic concentration and atomic ratios of the supports, determined by XPS.

Support	Surface atomic concentration				Surface atomic ratio		
	Ce (at%)	Hf (at%)	M (at%)	O (at%)	Ce/(Hf) ^a	M/(Ce + Hf) ^a	O/(Ce + Hf + M)
CH-Tb	20.14	8.12	2.34	64.41	2.48 (2.6)	0.08 (0.11)	2.10
CH-Sm	19.47	7.87	1.68	68.40	2.47 (2.6)	0.06 (0.11)	2.35
CH-Nd	18.38	7.66	1.72	64.06	2.40 (2.6)	0.07 (0.11)	2.30
CH-Pr	20.80	8.20	2.83	65.59	2.53 (2.6)	0.10 (0.11)	2.06
CH-La	21.29	8.53	2.17	66.95	2.49 (2.6)	0.07 (0.11)	2.09

^a Theoretical ratios are provided in parentheses.

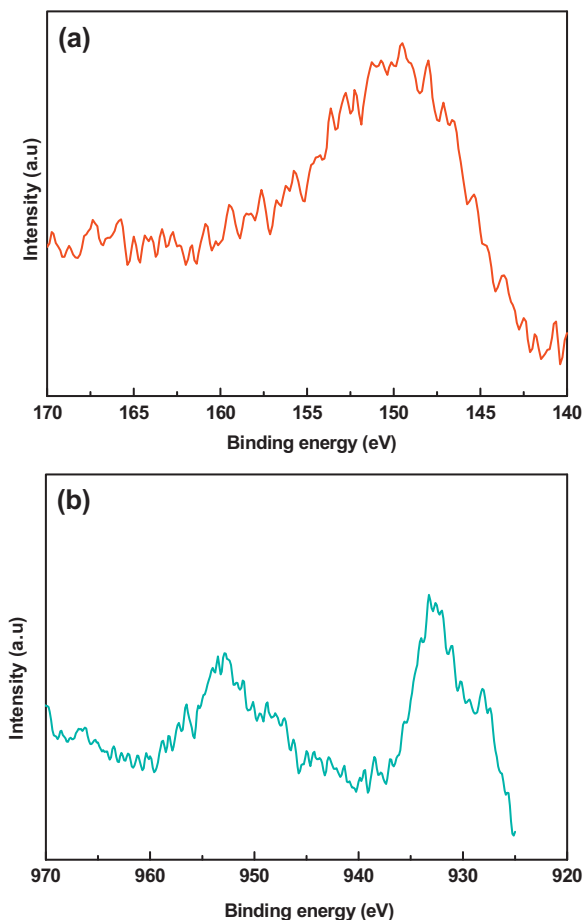


Fig. 5. XPS patterns of the M-doped CH materials (M = Tb and Pr) following calcination at 600 °C: (a) Tb 4d of CH-Tb and (b) Pr 3d of CH-Pr.

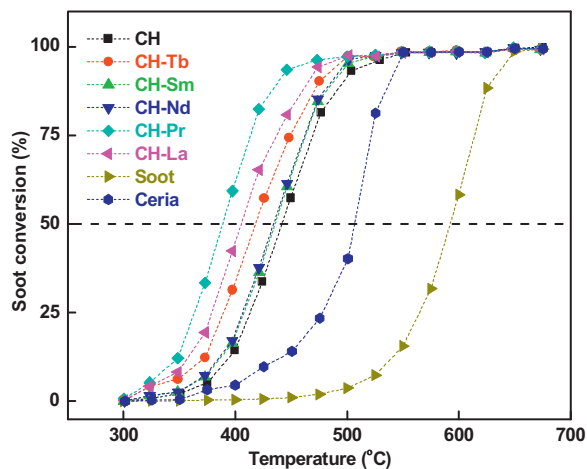


Fig. 6. Oxidation of pure soot, CeO₂, CZ, CH, and M-doped CH materials (M = Tb, Sm, Nd, Pr, La) under the flow of O₂ as a function of time.

Table 4
Light-off temperatures ($T_{1/2}$) of the supports for the soot oxidations.

Catalyst	$T_{1/2}$ (°C)
Soot	590
CeO ₂	508
CH	443
CH-Tb	418
CH-Sm	434
CH-Nd	436
CH-Pr	389
CH-La	404

reforming reactions occur at a catalyst supported on a metal oxide possessing a higher OSC, the active oxygen ions from the metal oxide support can easily react with carbon (soot) to form removable gases (e.g., CO₂) at a lower temperature. This carbon removal process would help suppress the deactivation of a catalyst through carbon coking during a reforming reaction. The light-off temperature ($T_{1/2}$) of a support, defined as temperatures at 50% conversion of soot [23], is thus correlated with the extent of OSC in the support;

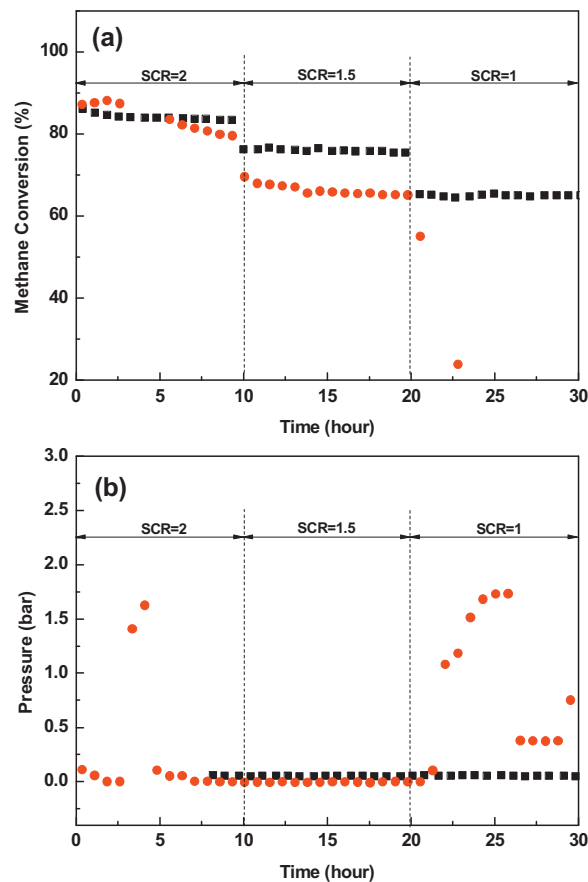


Fig. 7. Comparison for (a) methane conversion and (b) the inlet pressure of the micro-reactor over the Ni-based catalysts supported onto CH (Ni/CH, ●) and CH-Pr (Ni/CH-Pr, ■) for 30 h.

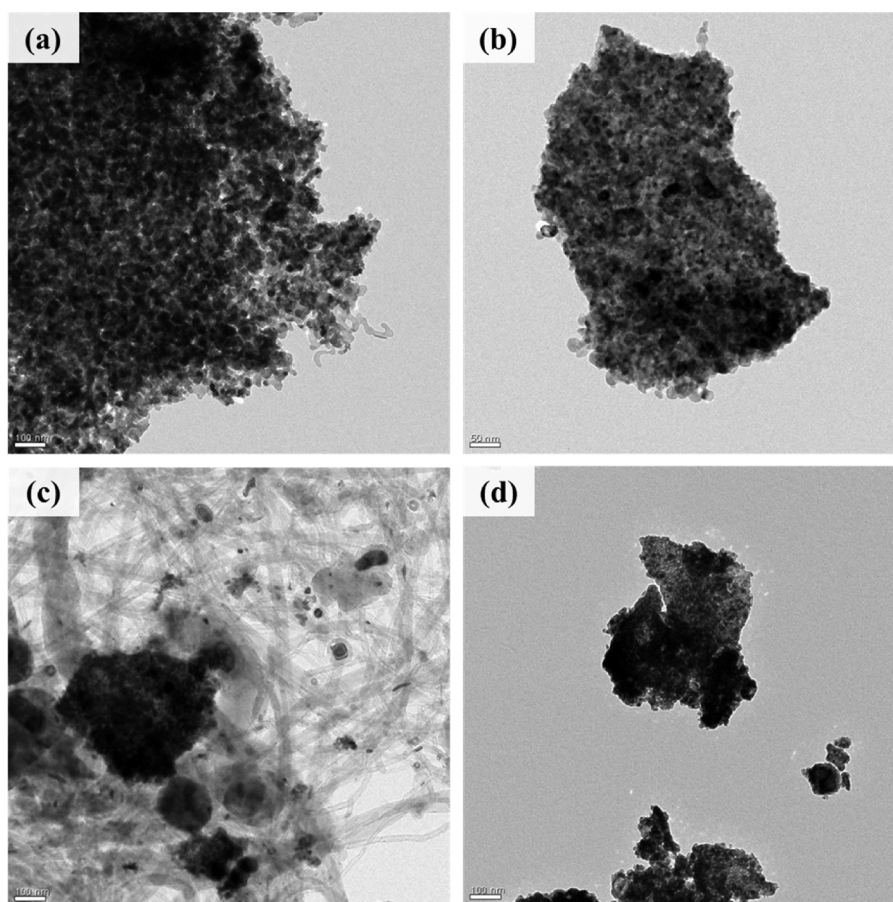


Fig. 8. TEM images of the used Ni-based catalysts after long-term test: (a) The fresh **Ni/CH** catalyst, (b) the **Ni/CH-Pr** catalyst, (c) **Ni/CH** (after SRM) (d) **Ni/CH-Pr** (after SRM).

i.e., a decrease in the $T_{1/2}$ temperature likely indicates an increased OSC of a support. In this context, we performed soot oxidation reactions in the presence of the as-synthesized metal oxide supports to determine their relative extent of OSC. Fig. 6 depicts the fraction of soot converted into gasified products (e.g., CO and CO₂) as a function of temperature. Compared to that for the soot oxidation in the absence of a support, the light-off temperatures ($T_{1/2}$) obtained with a support decreased in the following order: **CH-Pr** (389 °C) < **CH-La** (404 °C) < **CH-Tb** (418 °C) < **CH-Nd** (436 °C) ~ **CH-Sm** (434 °C) < **CH** (443 °C) < **CeO₂** (508 °C) < no metal oxide (590 °C). For CeO₂ and bare soot without metal oxide, the previously obtained data were inserted for comparison [41]. The $T_{1/2}$ values are summarized in Table 4. Compared to that without any metal oxide, the activity of ceria was previously reported to be higher for the soot oxidation due to the OSC of CeO₂ [42]. Our results revealed that the **CH** support had much higher OSC than ceria, and additional doping of the **CH** material with rare earth elements further enhanced OSC. In particular, **CH-Pr** showed the highest OSC among the materials employed in this study, which is consistent with the results obtained by Raman spectroscopy and XPS analyses (*vide supra*). This result suggests that the **CH** and **CH-M** supports can be beneficial to a reforming reaction requiring long-term stability against carbon-induced deactivation. To test this hypothesis, we prepared Ni catalyst supported onto the **CH-Pr** (with lowest light-off temperature for the soot oxidation) and **CH** supports and their activities towards steam reforming of methane (SRM) were then compared; if the hypothesis is true, a Ni-based catalyst with this **CH-Pr** support would be more stable than **CH** under the same SRM conditions (*vide infra*).

3.6. Measurement of the OSC values of the as-developed materials: Thermogravimetric analyses

The obtained relative extent of OSC using soot oxidation could provide valuable information about the activity and stability of reforming reactions. However, the soot oxidation experiments are likely dependent upon the surface area of a material since they involve reactions between (soot+materials) and oxygen. In this context, thermogravimetric analyses were performed to determine the OSC values of **CH-M** directly. The OSCs obtained at 750 °C were found to increase in the following order (Table S1): **CH-Tb** (17.0 mmol-O₂/mol) > **CH-Pr** (13.8 mmol-O₂/mol) ~ **CH-La** (13.6 mmol-O₂/mol) > **CH-Sm** (10.8 mmol-O₂/mol) > **CH-Nd** (6.2 mmol-O₂/mol) > **CH** (3.6 mmol-O₂/mol). The relative extents of OSC determined by the thermogravimetric analyses were slightly different from those obtained by the soot oxidation results (**CH-Pr** > **CH-La** > **CH-Tb** > **CH-Sm** ~ **CH-Nd** > **CH**, Table 4). This difference likely originates from the different surface areas of the **CH-M** supports; i.e., the measured surface area of **CH-Tb** was found to be lower compared to those of **CH-Pr** and **CH-La** (Table 1), which afforded the slightly lower extent of OSC than those of **CH-Pr** and **CH-La** upon determination with soot oxidation.

The OSC values were further found to be dependent upon temperatures. When the OSCs of **CH-M** (M = La, Tb, and Pr) were measured as a function of temperature in the range from 550 °C to 750 °C, they increased as temperature increased (Fig. S2 and Table S2). The **CH-La** material showed highest OSC at 650 °C among the metal oxides employed while **CH-Tb** exhibited the highest OSC at

750 °C. Notably, the determined OSCs of these materials at 550 °C were found to be higher than that of CH obtained at 750 °C.

3.7. Durability of Ni-based catalysts supported on CH-Pr for SRM

The obtained results described above suggest that a catalyst supported onto a material possessing improved OSC by incorporating Pr into the CH material would be beneficial to maintain its catalytic durability against carbon coking because the material can suppress catalyst deactivation by delivering oxygen ions into carbon species to yield gasified products (e.g., CO₂). To determine relative stability of a catalyst for a reaction involving carbon coking, Ni/CH and Ni/CH-Pr catalysts were prepared and SRM was then performed over these catalysts at 700 °C for a period of 30 h (10 h for each S/C ratio). To accelerate carbon formation on these catalysts, S/C ratios were changed from 2 to 1 with time. The Ni/CH-Pr catalyst showed good catalytic stability for the SRM reaction, and CH₄ conversions decreased stepwise from 84% to 65% upon decreasing S/C ratios (Fig. 7a), while the Ni/CH catalyst showed relatively lower catalytic activity than Ni/CH-Pr with a sudden drop in CH₄ conversion immediately following the reduction of the S/C ratio from 1.5 to 1. Notably, the significant drop in CH₄ conversion of Ni/CH with the S/C ratio of 1 is in line with the rapid pressure build-up in the inlet of the reactor due to carbon clogging (Fig. 7b). These results suggest that the carbon species deposited onto Ni/CH was not successfully removed to lead to the catalyst deactivation while the increased OSC of the CH-Pr support likely induced facile gasification of the deposited carbon on Ni/CH-Pr to maintain its activity.

Consistent with this observation, severe carbon formation was found at the surface of the Ni/CH catalyst (Fig. 8). TEM images obtained after the SRM reaction with Ni/CH revealed the significant formation of filamentous carbon deposits on its surface (Fig. 8c). In contrast, no visible carbon species was found in the Ni/CH-Pr catalyst (Fig. 8d). These results clearly indicate that compared to Ni/CH, the Ni catalyst supported onto CH-Pr possessing high OSC helped suppress the carbon formation. In addition, carbon coking appears to be a favored process over metal sintering for catalyst deactivation under the conditions employed in this study. The enhanced oxygen ion conductivity (or OSC) thus played a crucial role in improving the stability of the Ni-based catalyst

3.8. Measurement of weight change

To examine the influence of OSC on carbon formation, TGA analyses were further performed on the Ni/CH and Ni/CH-Pr catalysts

using only CH₄ at 700 °C with a methane flow rate of 200 mL/min. During the methane cracking reaction (CH₄ → C + H₂), increases in weight of the catalysts are expected due to the carbon formation. These changes were recorded for 1200 min upon methane cracking over two catalysts, Ni supported onto CH and CH-Pr. It is evident that the rate of weight gain with Ni/CH-Pr was found to be lower when compared to the Ni/CH catalyst (Fig. 9). These results are again originated from the enhanced OSC of the CH-Pr support that helped oxidize the deposited carbon species at the surface of the Ni catalyst.

4. Conclusions

In summary, the rare earth metal-doped CeO₂-HfO₂ materials (Ce_{0.65}Hf_{0.25}M_{0.1}O_{2-δ}, M = Tb, Sm, Nd, Pr, and La) were synthesized and characterized by XRD, BET, Raman spectroscopy, XPS, and TEM methods. These solid solutions exhibited cubic fluorite structure with particle sizes in a range of 11–16 nm. Raman spectroscopy, XPS studies, and soot oxidation disclosed that the doped CH-M materials had an increased quantity of oxygen vacancies compared to the undoped CH solid solution, and among the doped materials, the CH-Pr, CH-La, and CH-Tb materials were suggested to possess superior oxygen storage capacities. Finally, studies employing the Ni-based catalysts supported onto CH and CH-Pr for catalytic steam reforming of methane proved that Ni/CH-Pr had increased activity and stability compared to Ni/CH upon utilization of S/C ratios of 1–2 at 700 °C. The doping strategy using a rare earth element presented herein is beneficial to tune the OSC of metal oxides for a number of catalytic applications. In addition, the identified controlling factors to enhance the OSC of a metal oxide would further provide valuable insights to develop highly durable catalytic materials for hydrogen production that can readily be achieved by various chemical transformations.

Acknowledgements

This research was supported by the Global Research Laboratory Program through the National Research Foundation of Korea funded by the Ministry of Science, ICT and Future Planning of Republic of Korea. Part of this research was also supported by the Fundamental Technology Development Programs for the Future through the Korea Institute of Science and Technology.

Appendix A. Supplementary data

Supplementary data associated with this article can be found, in the online version, at <http://dx.doi.org/10.1016/j.apcatb.2013.11.022>.

References

- [1] J. Kašpar, P. Fornasiero, M. Graziani, *Catal. Today* 50 (1999) 285–298.
- [2] A. Lashtabeg, S.J. Skinner, *J. Mater. Chem.* 16 (2006) 3161–3170.
- [3] D. Hari Prasad, H.I. Ji, H.R. Kim, J.W. Son, B.K. Kim, H.W. Lee, J.H. Lee, *Appl. Catal., B* 101 (2011) 531–539.
- [4] H. Kušar, S. Hočevár, J. Levec, *Appl. Catal., B* 63 (2006) 194–200.
- [5] V.V. Kharton, A.A. Yaremchenko, E.N. Naumovich, F.M.B. Marques, *J. Solid State Electrochem.* 4 (2000) 243–266.
- [6] R. Si, Y.-W. Zhang, L.-M. Wang, S.-J. Li, B.-X. Lin, W.-S. Chu, Z.-Y. Wu, C.-H. Yan, *J. Phys. Chem. C* 111 (2006) 787–794.
- [7] J. Mikulová, S. Rossignol, J. Barbier Jr., D. Duprez, C. Kappenstein, *Catal. Today* 124 (2007) 185–190.
- [8] B.M. Reddy, P. Lakshmanan, P. Bharali, P. Saikia, G. Thirumurthulu, M. Muhler, W. Grünert, *J. Phys. Chem. C* 111 (2007) 10478–10483.
- [9] B.M. Reddy, P. Saikia, P. Bharali, Y. Yamada, T. Kobayashi, M. Muhler, W. Grünert, *J. Phys. Chem. C* 112 (2008) 16393–16399.
- [10] B.M. Reddy, P. Saikia, P. Bharali, S.-E. Park, M. Muhler, W. Grünert, *J. Phys. Chem. C* 113 (2009) 2452–2462.

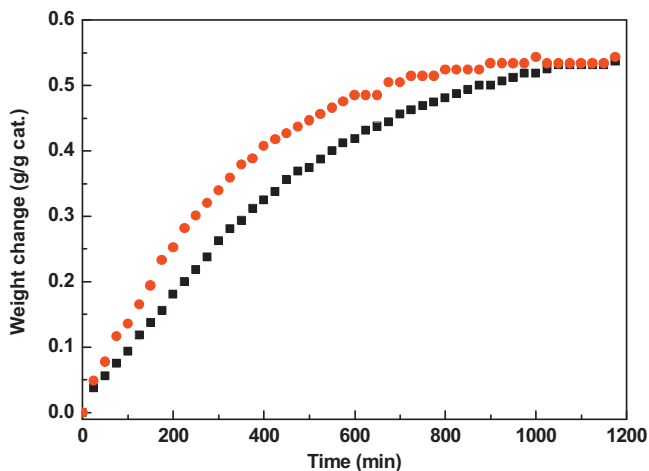


Fig. 9. Weight changes of Ni/CH (●) and Ni/CH-Pr (■) during exposure to methane for 1200 min.

- [11] B.M. Reddy, G. Thrimurthulu, L. Katta, Y. Yamada, S.-E. Park, *J. Phys. Chem. C* 113 (2009) 15882–15890.
- [12] B.M. Reddy, G. Thrimurthulu, L. Katta, *Catal. Today* 175 (2011) 585–592.
- [13] B.M. Reddy, G. Thrimurthulu, L. Katta, *Chem. Mater.* 22 (2010) 467–475.
- [14] M. Sugiura, *Catal. Surv. Asia* 7 (2003) 77–87.
- [15] A. Trovarelli, *Catalysis by Ceria and Related Materials*, Imperial College Press, London, 2002.
- [16] B.M. Reddy, P. Bharali, P. Saikia, A. Khan, S. Loidant, M. Muhler, F. Grünert, *J. Phys. Chem. C* 111 (2007) 1878–1881.
- [17] G. Zhou, R. Gorte, *J. Phys. Chem. B* 112 (2008) 9869–9875.
- [18] B.M. Reddy, G. Thrimurthulu, L. Katta, *Catal. Lett.* 141 (2011) 572–581.
- [19] B.M. Reddy, P. Bharali, P. Saikia, *J. Phys. Chem. C* 112 (2008) 11729–11737.
- [20] H. Gu, R. Ran, W. Zhou, Z. Shao, *J. Power Sources* 172 (2007) 704–712.
- [21] D. Harshini, C.W. Yoon, J. Han, S.P. Yoon, S.W. Nam, T.-H. Lim, *Catal. Lett.* 142 (2012) 205–212.
- [22] B.M. Reddy, K.N. Rao, *Catal. Commun.* 10 (2009) 1350–1353.
- [23] Y. Kim, J.H. Kim, J. Bae, C.W. Yoon, S.W. Nam, *J. Phys. Chem. C* 116 (2012) 13281–13288.
- [24] S.V. Moharil, B.S. Nagrare, S.P.S. Shaikh, *Int. J. Hyd. Energy* 37 (2012) 5208–5215.
- [25] W.-C. Wu, J.-T. Huang, A. Chiba, *J. Power Sources* 195 (2010) 5868–5874.
- [26] Y. Tao, J. Shao, J. Wang, W.G. Wang, *J. Power Sources* 185 (2008) 609–614.
- [27] M.F. Wilkes, P. Hayden, A.K. Bhattacharya, *J. Catal.* 219 (2003) 305–309.
- [28] S. Zhao, R.J. Gorte, *Appl. Catal., A* 277 (2004) 129–136.
- [29] X. Wu, X. Wu, Q. Liang, J. Fan, D. Weng, Z. Xie, S. Wei, *Solid State Sci.* 9 (2007) 636–643.
- [30] D. Hari Prasad, S.Y. Park, H.-I. Ji, H.-R. Kim, J.-W. Son, B.-K. Kim, H.-W. Lee, J.-H. Lee, *J. Phys. Chem. C* 116 (2012) 3467–3476.
- [31] R.D. Monte, J. Kašpar, *J. Mater. Chem.* 15 (2005) 633–648.
- [32] W.Y. Hernández, M.A. Centeno, F. Romero-Sarria, J.A. Odriozola, *J. Phys. Chem. C* 113 (2009) 5629–5635.
- [33] J.R. McBride, K.C. Hass, B.D. Poindexter, W.H. Weber, *J. Appl. Phys.* 76 (1994) 2435–2441.
- [34] M.-F. Luo, Z.-L. Yan, L.-Y. Jin, M. He, *J. Phys. Chem. B* 110 (2006) 13068–13071.
- [35] M. Guo, J. Lu, Y. Wu, Y. Wang, M. Luo, *Langmuir* 27 (2011) 3872–3877.
- [36] F. Le Normand, J. El Fallah, L. Hilaire, P. Légaré, A. Kotani, J.C. Parlebas, *Solid State Commun.* 71 (1989) 885–889.
- [37] D.R. Mullins, S.H. Overbury, D.R. Huntley, *Surf. Sci.* 409 (1997) 307–319.
- [38] C.D. Wagner, W.M. Riggs, L.E. Davis, J.F. Moulder, in: G.E. Muilenberg (Ed.), *Handbook of X-ray Photoelectron Spectroscopy*, Perkin-Elmer Corporation, Minnesota, 1978.
- [39] H. He, H.X. Dai, C.T. Au, *Catal. Today* 90 (2004) 245–254.
- [40] A. Galtayries, R. Sporken, J. Riga, G. Blanchard, R. Caudano, *J. Electron Spectrosc. Relat. Phenom.* 88–91 (1998) 951–956.
- [41] D. Harshini, Y. Kim, S.W. Nam, T.-H. Lim, S.-A. Hong, C.W. Yoon, *Catal. Lett.* 143 (2013) 49–57.
- [42] A. Bueno-López, K. Krishna, M. Makkee, J.A. Moulijn, *Catal. Lett.* 99 (2005) 203–205.